JOURNAL OF SPACECRAFT AND ROCKETS
Vol. 42, No. 3, May–June 2005

Multibody Dynamics Modeling of Segmented Booms of the Mars Express Spacecraft

Edward Mettler* and Marco B. Quadrelli†
Jet Propulsion Laboratory, California Institute of Technology, Pasadena, California 91109-8099

We provide an independent modeling and dynamic analysis of the antenna segmented booms deployed on the Mars Express Spacecraft. The Mars Express Spacecraft, built by the ESA, was launched in June 2003 and arrived at Mars in December 2003 to begin a four-year study of the planet's atmosphere, surface, and subsurface. The Mars Advanced Radar for Subsurface and Ionospheric Mapping is a key instrument in the search for water on Mars. Our objective was to determine the antenna's dynamic interaction with the spacecraft bus. Numerical simulations of a model of the spacecraft in the perigee phase of its elliptical Mars orbit were performed, with all booms fully deployed and reaction wheels used to both disturb and control the spacecraft attitude. The simulation results verify the antenna system modeling fidelity and provide data on worst-case dynamic interactions between the flexible booms and the spacecraft bus that demonstrates the dynamic compatibility with the spacecraft.

Nomenclature

a	=	semimajor axis, m
a_J	=	non-rigid-body mode coefficients, with $J = 1, 2, 3, \ldots, n$
$\boldsymbol{d}$	=	nodal displacement, m
E	=	modulus of elasticity, N/m^2
e	=	eccentricity
$\boldsymbol{F}$	=	vector of generalized forces
F_I	=	Mars-centric inertial inertial reference frame, $=(X, Y, Z)$
$F_{\text{ORF}}(x, y, z)$	=	local vertical-local horizontal (LV-LH) orbiting reference frame (ORF)
$\boldsymbol{f}_a$	=	actuation force vector, N
$\boldsymbol{f}_e$	=	generalized structural force caused by material elasticity, N
$\boldsymbol{f}_J$	=	natural frequencies of homogeneous cantilever beams, rad/s
$\boldsymbol{f}_R, f_r, f_t$	=	vector of generalized (reduced) external forces on the appendage nodes, N
$\boldsymbol{f}_r$	=	vector of the wheel disturbance forces and torques on the bus, plus the reaction wheel actuation torques, N
$\boldsymbol{f}_1$	=	vector of external forces at node 1, N
$\boldsymbol{G}^i(\boldsymbol{H}^w)$	=	skew-symmetric gyroscopic matrix
$\boldsymbol{g}$	=	vector of generalized gyroscopic and external forces, N
$\boldsymbol{h}_i$	=	internal angular momentum of wheels, kgm^2/s
I	=	area moment of inertia of beam about the neutral axis, m^2
i	=	inclination
$\boldsymbol{J}_w^w$	=	diagonal matrix of wheel axial inertia
$\boldsymbol{J}^1$	=	spacecraft moment of inertia matrix about center of mass, kgm^2
$\boldsymbol{K}_{ij}$	=	spring constant including the effect of the rotational spring at the hinge and root, Nm/rad
$\boldsymbol{K}_p, \boldsymbol{K}_v$	=	translation control gain matrices, Nm/rad
K_{ry}, K_{rz}	=	stiffness of the boom "root" in the two transverse directions, Nm/rad
L	=	length of beam, m
$L(\boldsymbol{\eta}, \dot{\boldsymbol{\eta}}, t)$	=	Lagrangian of S, Js
M	=	mass per unit length of beam, kg/m
$\boldsymbol{M}^1$	=	mass matrix of node 1 of the bus, kg
M_{re}	=	coupling inertia term, kg
$\boldsymbol{M}_t$	=	block diagonal mass matrix, kg
$\boldsymbol{M}^i$	=	spacecraft mass matrix, kg
m_i	=	mass of ith body/node, kg
N_b	=	number of bodies
n_e, n_g	=	number of independent and global set of degrees of freedom, respectively
n_t	=	total number of degrees of freedom of each elastic segment times the number of segments
$\boldsymbol{P}_{1[n\times m]}$	=	orthogonal complement of $\boldsymbol{\Phi}_q^T$
$\boldsymbol{P}_{2[n\times(n-m)]}$	=	matrix in the null space of $\boldsymbol{\Phi}_q$
$\boldsymbol{p}^i_{\text{est}}, \boldsymbol{p}^i_{\text{cmd}}$	=	estimated and commanded translation state, m
$\boldsymbol{q}$	=	(of length $n_g + 1$) vector containing the nodal displacements and rotations of each node in global coordinates plus the reaction wheel rotation angles plus the degrees of freedom of the bus
$\boldsymbol{q}_i$	=	quaternion parameters
$\boldsymbol{q}_r, \boldsymbol{q}_t$	=	vector containing the reduced nodal and total displacements and rotations of each node in global coordinates, respectively
$\boldsymbol{R}$	=	rotation matrix of ORF to inertial frame
R_0	=	orbital semimajor axis, m
$\boldsymbol{R}_0$	=	orbital radius vector to origin of ORF, m
$\boldsymbol{r}_i$	=	position vector of the center of mass of ith body
$\boldsymbol{S}^1$	=	first moment of inertia matrix of node 1 of the bus, kgm
$\boldsymbol{T}$	=	transformation matrix of dimension $n_g \times n_e$
$\boldsymbol{u}$	=	vector of nodal external forces and moments
$\boldsymbol{v}_i$	=	velocity vector of the center of mass of ith body, m/s
$\boldsymbol{X}$	=	system state vector
$\boldsymbol{x}$	=	state vector as $\boldsymbol{x} = (\boldsymbol{\eta}, \boldsymbol{\beta}, \boldsymbol{\eta}, \boldsymbol{\Omega})^T$
α	=	angular acceleration, rad/s^2
β	=	reaction-wheel angle, rad

Presented as Paper 03-0156 at the AAS/AIAA 13th Spaceflight Mechanics Meeting, Ponce, PR, 9–13 February 2003; received 9 September 2003; revision received 7 April 2004; accepted for publication 8 April 2004.

*Senior Engineer. Senior Member AIAA.
†Senior Engineer, Mail Stop 198-326; Marco.B.Quadrelli@jpl.nasa.gov. Senior Member AIAA.

$\boldsymbol{\Gamma}_p, \boldsymbol{\Gamma}_v$ = rotational control gain matrices, Nm/rad
$\boldsymbol{\Gamma}(\boldsymbol{q}_i)$ = mapping from angular velocity vector to attitude parameters
$\boldsymbol{\gamma}(t)$ = constraint terms in accelerations
$\boldsymbol{\eta}$ = vector of generalized coordinates and speeds
θ_{err} = magnitude of rotation corresponding to the difference between the commanded and the estimated quaternion, rad
θ_w = reaction wheel angles, rad
$\boldsymbol{\theta}_{\delta i}$ = virtual variation of the quasi-coordinate describing the rotation
$\boldsymbol{\Lambda}$ = diagonal matrix of natural frequencies, rad/s
λ = eigenaxis of rotation
$\boldsymbol{\lambda}$ = vector of Lagrange multipliers
μ_M = Mars gravitational parameter, m^3/s^2
ν = true anomaly, rad
$\boldsymbol{\nu}(\boldsymbol{t})$ = constraint terms in velocities
ξ = modal damping coefficient
$\boldsymbol{\rho}_i$ = relative position vector of body i wrt ORF, m
$\boldsymbol{\sigma}$ = vector of generalized momenta
$\boldsymbol{\tau}_a, \boldsymbol{\tau}_e, \boldsymbol{\tau}_1$ = actuator torques, generalized torques caused by material elasticity, and external perturbation and control torques, Nm
$\boldsymbol{\tau}_w, \boldsymbol{\tau}_w^w$ = reaction wheel control torque, Nm
Φ = constraint Jacobian
$\boldsymbol{\varphi}$ = modal matrix
Ω = orbital mean motion, rad/s
$\boldsymbol{\Omega}$ = wheel rate vector, rad/s
Ω_L = longitude of ascending node, rad
ω = argument of perigee, rad
$\boldsymbol{\omega}, \omega_i$ = angular velocity vector, rad/s
$\mathbf{1}_n$ = (n, n) identity matrix

Introduction

THIS paper provides an independent modeling and dynamic analysis of the Mars Advanced Radar for Subsurface and Ionospheric Mapping (MARSIS) antenna segmented booms deployed on the Mars Express Spacecraft.[‡] This work was done to establish the highest confidence for the antenna system in-flight dynamics compatibility with the Mars Express mission.

The Mars Express Mission is a joint NASA/ESA cooperative project. The Mars Express Spacecraft built by ESA will study Mars for about four years from a highly elliptical orbit (15,000-km apoapsis and 250-km periapsis altitude) with seven major science instruments on the spacecraft plus a small lander vehicle, named Beagle 2. The mission was launched in June 2003 and arrived at Mars in December 2003. The Mars Advanced Radar for Subsurface and Ionospheric Mapping instrument, provided by NASA and managed by the Jet Propulsion Laboratory, is a key instrument in the search for water on Mars, and is a four-frequency band synthetic aperture altimeter with penetration capability for subsurface and atmospheric sounding from 40-m-long dipole antennas oriented parallel to the planet surface and a 7-m-long monopole along the nadir for clutter cancellation.

The objective of this work was to determine the antenna's dynamic interaction with the spacecraft bus (or central rigid body). Static and modal analyses make use of boom material parameters, mass properties, and laboratory test results provided by TRW, Inc., in addition to data provided by the European consortium Astrium on spacecraft mass properties and orbital parameters. Solutions are derived involving coupled equations of motion for vehicle orbital mechanics, rigid-body spacecraft bus, and flexible-appendages dynamics. Numerical simulations were performed of a "flying model" of the spacecraft in the perigee phase of its elliptical Mars orbit, with all MARSIS booms fully deployed and reaction wheels used to both disturb and control the spacecraft attitude. The spacecraft's reaction-wheel model and attitude controller were designed by the authors and were not optimized or based on any specific information provided by Astrium. Realistic excitations of the bus and boom appendages were imposed by short reaction-wheel torque-time profiles that were constructed to maximize excitation of the system fundamental vibration mode. To clearly identify only the MARSIS interaction with the bus, the solar panels were modeled as rigid elements, and the attitude sensors and reaction wheels were assumed to be free from noise and other errors. The simulation results verify the Antenna system modeling fidelity and provide data on approximate worst-case dynamic interactions between the flexible booms and the spacecraft bus that demonstrate the MARSIS dynamic compatibility with the spacecraft.

Previous related works on modeling of multibody flexible booms mounted on spacecraft have addressed the in-flight disturbances and dynamic response of Earth orbiters,[1] general approaches for efficient modeling[2] and control methodologies,[3] interaction of boom dynamics with high-precision pointing using reaction wheels,[4] and boom modeling for inflatable telescopes.[5] In this paper, we describe how the multibody modeling of segmented booms and pointing analysis with reaction wheels of MARSIS was carried out by using limited information available on the structural dynamics.

First, we describe the modeling approach. Second, we describe the equations of motion and the component model reduction procedure to obtain reduced-order model equations of motion of the system. Third, we describe the control laws used to point the spacecraft in orbit around Mars at the perigee. A discussion of the numerical results concludes the paper.

Approach to Dynamic Analysis and Modeling

Clearly, the MARSIS uniquely segmented booms present a dynamic modeling challenge and a special problem in predicting the on-orbit deployed dynamic behavior. For the Mars Express mission, where a precise attitude-pointing stability prediction is required, the solution needs to include the segmented dipole and monopole antennas flexible boom appendages, the attachment boundary conditions, and the rigid-body inertial dynamics of the spacecraft in its Martian elliptical orbit with orbital mechanics, gravity-gradient torques, and closed-loop reaction-wheel control. The following modeling, analysis, and simulations were performed with this approach. In the deployed state, the appendage model is far from being a uniform, homogeneous beam. Rather, it consists of 13 segments hinged together by some kinematic constraints. This motivates the multibody analysis to be discussed next.

Assumptions of the Dynamic Model

A dynamic model of the deployed dipole and monopole booms was derived under the following assumptions. Only a small portion of the orbit is simulated, that is, 100 s representing the spacecraft's periapsis passage in its elliptical Mars orbit. The spacecraft bus is modeled as a rigid body with three reaction wheels aligned along the principal axes. The spacecraft attitude control system is deliberately modeled with perfect position and rate reference sensors. (Reaction wheels are modeled with realistic rotor inertia, momentum storage, and torque capabilities.) The solar panels are deliberately modeled as rigid fixed elements, and their inertia contribution is included in the moment of inertia matrix of the bus about its center of mass. This approximation is done to avoid additional complications in the model, but primarily because the solar panels are much stiffer than the antenna. (Specific data on the solar panels was not provided by the spacecraft manufacturer, only the knowledge that the first fundamental frequency of the solar panels is well above the reaction wheel control bandwidth, and hence unimportant for the present analysis.) The vehicle dynamics are coupled to the orbital dynamics, but the spacecraft undergoes only small rotational motions of less than 1 deg. The monopole and dipole booms were first modeled as cantilever beams of uniform and homogeneous material properties along their length. However, we were not able to duplicate the experimental results provided by TRW. An improved equivalent model was derived assuming that each boom is modeled as a serial chain of hinged flexible beams, with rotational springs at the "root" (attachment point to the bus) and between the segments. The root

[‡]Data available online at http://www.esa.int/SPECIALS/Mars_Express/SEMUC 759ED_0.html.

spring constants are obtained from the TRW static deflection water tank (0-g) tests. The rotational spring constants between each hinged segment are kept as free parameters in order to match the first mode of the tested article. The hinges are modeled as perfect spherical joints.

Boom-Bus Attachment Boundary Condition Influence

Next, we present comparative information showing the dynamic behavior that supports the conservatism of using fixed-free or various degrees of fixity, such as root hinge stiffness, vs the actual in-space condition of quasi-free–free boundaries seen by the MARSIS booms. The term "quasi" is used to express that the spacecraft central body mass and rotational inertia will impose force and moment constraints on the boom root interface. If the central body were massless, then a true free–free boundary condition would be present for the booms. The following approximate functional relationship from Harris[6] provides an insight into boundary condition influence on the natural frequencies (in [rad/s]) of homogeneous cantilever beams:

$$f_J = \left[a_J^2 / L^2\right](EI/m)^{\frac{1}{2}} \tag{1}$$

where the a_J are iteratively derived from transcendental hyperbolic equations for homogeneous cantilever beams, with $J = 1, 2, 3, \ldots, n$. Then, comparing the two extreme cantilever beam boundary conditions of fixed–free vs free–free, the first four mode coefficients a_J are shown in Table 1. One can readily see the ratio of the $(a_J)^2$ terms for two boundary conditions provides modal frequency scaling, for example, the first modes will have $(4.7300)^2/(1.8751)^2 = 6.364/1$. Thus the pure free–free beam fundamental frequency will be 6.364 times higher than the fixed–free beam fundamental frequency. Similar results are obtained by Woodard et al.[1] on beams with tip inertias. Although these facts provide a conservative direction for TRW's results, they do not allow accurate prediction of the actual in-flight dynamics of the segmented MARSIS booms. It is clear, however, that the finite stiffness of the root hinge is not a fixed or clamped case and tends towards a free–free case or higher frequency. Mitigating that are the segment spliced joints, which tend to lower the overall boom stiffness.

Table 1 Mode coefficients of fixed-free and free–free beams

Mode number	Fixed (or clamped)–free	Free–free
1	1.8751	4.7300
2	4.6941	7.8532
3	7.8547	10.9956
4	10.9955	14.1371

Boom Stiffness Symmetry

TRW conducted static load-deflection water tank (near 0-g) tests of the fully deployed 20-m boom to determine the global bending transverse stiffness, the stiffness of the boom root in the two transverse directions K_{ry} and K_{rz} and also to obtain data on the stiffness of the spliced joints. The x direction is defined as the roll axis, whereas the y and z axes are the yaw and pitch axes, respectively. The root stiffness K_{ry} was found to be 926.47 N-m/rad, and K_{rz} was 206.76 N-m/rad. Thus, the root section was 4.48 times stiffer in the y direction, which is not surprising because the slotting of the boom tube at the segment fold points creates an obvious asymmetry. The test data also indicated the stiffness of the typical spliced section was 2.6 times greater in the z direction than the y direction. This result is opposite to the root stiffness asymmetry and leads to the expectation that the combined segmented boom deflections caused by root and splices will tend to cancel out local differences in directionality for the global boom behavior. These static deflection tests also indicated reasonable transverse symmetry for the global stiffness that was later confirmed by the symmetric frequencies obtained from the TRW 10-m free–fixed boom scaled impulse response dynamic tests. We have therefore taken this into account in this analysis and detailed modeling of the segments and joints and assumed approximately the same global stiffness and natural frequencies in both transverse directions of the fully deployed booms.

Equations of Motion

The equations of motion of the entire system will be derived in this section. We refer to Fig. 1. We introduce the Mars-centric inertial inertial reference frame F_I: X pointing toward the vernal equinox, Z toward the north pole, and Y completes the right-handed reference frame and the orbiting reference frame F_{ORF}, which we use to describe the near-field dynamics of the spacecraft relative to its orbit. This reference frame is attached to a point that follows a Keplerian orbit around the primary body. The motion of the system is then described with respect to a local-vertical local-horizontal (LVLH) orbiting reference frame $(x, y, z) = F_{\mathrm{ORF}}$ of origin O_{ORF}, which rotates with mean motion Ω and orbital semimajor axis R_0, z along the local vertical, x toward the flight direction, and y in the orbit normal direction. The orbital dynamics equation for point O_{ORF} is propagated forward in time under the influence of the gravitational

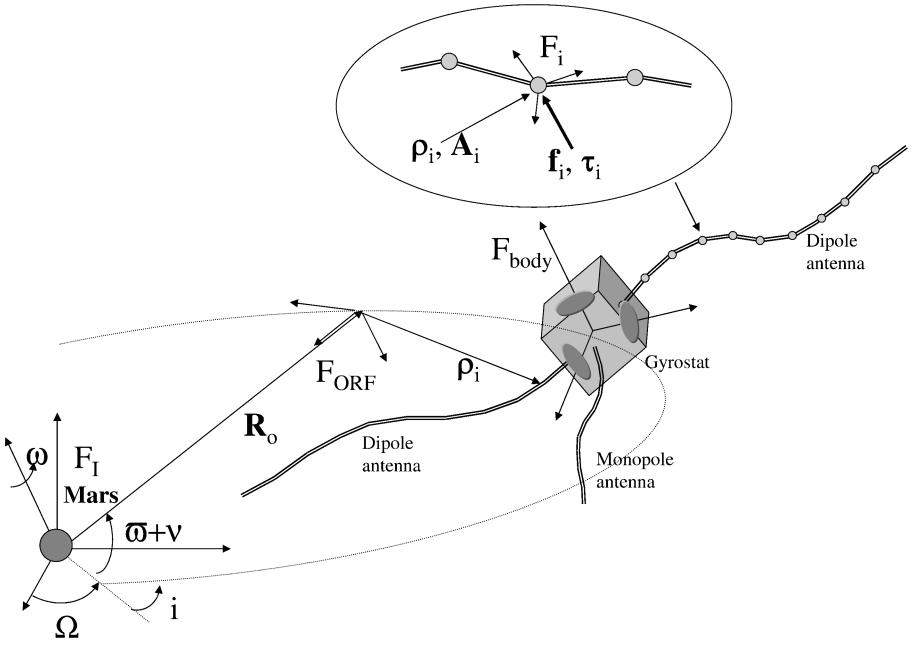

Fig. 1 Geometry of MARSIS dynamic model.

field of Mars. The origin of this frame coincides with the initial position of the center of mass of the system. The orbit of the origin of F_{ORF} is defined by the six orbital elements a, e, i, Ω_L, ω, ν, and time of passage through periapsis. From Fig. 1, the position vector of a generic structural point with respect to O_{ORF} is denoted by $\boldsymbol{\rho}_i$, and we have $\boldsymbol{r}_i = \boldsymbol{R}_0 + \boldsymbol{\rho}_i$. We define the state vector as $\boldsymbol{X} = (\boldsymbol{R}_0, \boldsymbol{V}_0, \boldsymbol{\rho}_1, \boldsymbol{q}_1, \boldsymbol{v}_1, \boldsymbol{\omega}_1, \ldots, \boldsymbol{\rho}_N, \boldsymbol{q}_N, \boldsymbol{v}_N, \boldsymbol{\omega}_N, \theta_1, \theta_2, \theta_3, \omega_1, \omega_2, \omega_3)^T$. The kinematics equations are as follows:

$$\boldsymbol{v}_i = \dot{\boldsymbol{\rho}}_i, \qquad \boldsymbol{\omega}_i = \boldsymbol{\Gamma}(\boldsymbol{q}_i)\dot{\boldsymbol{q}}_i, \qquad \boldsymbol{\omega}_w = \dot{\boldsymbol{\theta}}_w \tag{2}$$

The translation dynamics equations are as follows.
Near field:

$$\ddot{\boldsymbol{\rho}}_i = -\ddot{\boldsymbol{R}}_0 - \boldsymbol{\Omega} \times \boldsymbol{\Omega} \times \boldsymbol{\rho}_i - 2\boldsymbol{\Omega} \times \dot{\boldsymbol{\rho}}_i + \ddot{\boldsymbol{r}}_i \tag{3}$$

Far field:

$$\ddot{\boldsymbol{r}}_i = -\mu_M \left(\boldsymbol{r}_i \big/ |\boldsymbol{r}_i|^3\right) + \boldsymbol{f}_a/m_i + \boldsymbol{f}_e/m_i \tag{4}$$

$$\ddot{\boldsymbol{R}}_0 = -\left(\mu_M \big/ R_0^3\right)\boldsymbol{R}_0 \tag{5}$$

Equation (5) describes the Keplerian orbital dynamics. The rotational dynamics equations are

$$\boldsymbol{J}^1\dot{\boldsymbol{\omega}} + \dot{\boldsymbol{h}} + \boldsymbol{\omega} \times (\boldsymbol{J}^1\boldsymbol{\omega} + \boldsymbol{h}) = +\boldsymbol{\tau}_e + \boldsymbol{\tau}_a \tag{6}$$

$$\dot{\boldsymbol{h}} = -\boldsymbol{\tau}_w \tag{7}$$

The combined model of the bus plus appendages is based on eliminating the constraint reaction forces and torques via finite element assembly. The disturbance models that we consider acting on the spacecraft bus are gravity, solar pressure, and actuator forces, and torques. Control inputs are reaction-wheel forces and torques.

Constrained Flexible-Body Dynamics

Hamilton's principle[2] states that for any kinematically admissible variation δ of the displacement and rotation fields, that is, allowed by the geometry of the motion, the following stationarity condition holds for a system S of Nb bodies:

$$\sum_{i=1}^{Nb} \int_i^{i+1} \mathrm{d}t[\delta L(\boldsymbol{\eta}, \dot{\boldsymbol{\eta}}, t) + F \cdot \delta\boldsymbol{\eta}] = [\boldsymbol{\sigma} \cdot \delta\boldsymbol{\eta}]_i^{i+1} \tag{8}$$

where $L(\boldsymbol{\eta}, \dot{\boldsymbol{\eta}}, t)$ is the Lagrangean of S. For simplicity, let us impose that $\delta\eta = 0$ at the boundaries of the time interval. The vectors $\boldsymbol{\eta}$, $\dot{\boldsymbol{\eta}}$, and $\boldsymbol{F}$ and are defined as follows: $\boldsymbol{\eta} = (\boldsymbol{r}_i, \boldsymbol{q}_i)$, $\delta\boldsymbol{\eta} = (\delta\boldsymbol{r}_i, \boldsymbol{\theta}_{\delta i})$, and $\boldsymbol{F} = (\boldsymbol{f}_i, \boldsymbol{\tau}_i)$. The vectors $\boldsymbol{f}_i$ and $\boldsymbol{\tau}_i$ include external perturbation and control forces. The virtual displacements $\delta\boldsymbol{r}_i$ and virtual rotations $\theta_{\delta i}$ are kinematically admissible as they satisfy any constraint equations imposed on body i, namely, if $\Phi_{ri} \cdot \delta\boldsymbol{r}_i + \Phi_{\theta} i \cdot \boldsymbol{\theta}_{\delta i} = 0$, where $\Phi = [\Phi_{ri}, \Phi_{\theta i}]$ represents the Jacobian of a certain algebraic constraint equation $\psi = \psi(\boldsymbol{\eta}, \dot{\boldsymbol{\eta}}, t) = 0$. Therefore, there exists a vector of Lagrange multipliers $\boldsymbol{\lambda}$ such that, for arbitrary admissible $\delta\boldsymbol{r}_i$ and $\boldsymbol{\theta}_{\delta i}$, the new equations of motion for body i can be written in matrix form as[2–4]

$$\begin{bmatrix} \boldsymbol{M} & \boldsymbol{\Phi}^T \\ \boldsymbol{\Phi} & 0 \end{bmatrix} \begin{pmatrix} \ddot{\boldsymbol{\eta}} \\ \boldsymbol{\lambda} \end{pmatrix} = \begin{pmatrix} \boldsymbol{g} \\ \gamma \end{pmatrix} \tag{9}$$

where

$$\boldsymbol{M} = \begin{bmatrix} \begin{bmatrix} m_i\mathbf{1}_3 & \mathbf{0} \\ \mathbf{0} & \boldsymbol{J}_i \end{bmatrix} & & \mathbf{0} \\ & \ddots & \\ \mathbf{0} & & \begin{bmatrix} m_j\mathbf{1}_3 & \mathbf{0} \\ \mathbf{0} & \boldsymbol{J}_j \end{bmatrix} \end{bmatrix} \tag{10}$$

$$\boldsymbol{\Phi} = \begin{bmatrix} \boldsymbol{\Phi}_{r_i} & 0 & \boldsymbol{\Phi}_{r_j} & 0 \\ 0 & \boldsymbol{\Phi}_{\theta_i} & 0 & \boldsymbol{\Phi}_{\theta_j} \end{bmatrix} \tag{11}$$

Either the dipole or monopole boom behaves as a multibody system. Each boom has been discretized in a number of beams connected by spherical joints and supporting tailored rotational springs. The joint at the root has an elastic restraint, as observed in the ground tests. If the appendage was a continuous member (a cantilevered beam, for instance) the equations of motion for each appendage in global coordinates can be written as $\boldsymbol{M}_g\ddot{\boldsymbol{q}} + \boldsymbol{K}_g\boldsymbol{q} = \boldsymbol{f}_R$, where the vector $\boldsymbol{q}$ (of length n_g) contains the nodal displacements and rotations in global coordinates.

In our analysis, we noticed that a better correlation with the experimental modal frequencies of each appendage (monopole and dipole booms) can be achieved if the appendage is modeled as a series of elastic Bernoulli–Euler beams connected serially to each other by spherical joints, each joint supporting a rotational spring (in each direction). Instead of the fixed boundary condition at the root, a spherical joint with the root hinge spring constants was used. The model of the appendage then becomes $\boldsymbol{M}_t\ddot{\boldsymbol{q}}_t + \boldsymbol{K}_t\boldsymbol{q}_t = \boldsymbol{f}_t$, where the vector $\boldsymbol{q}_t$ (of length n_t) contains the nodal displacements and rotations of each constrained node in global coordinates, and

$$\boldsymbol{K}_t = \begin{pmatrix} \boldsymbol{K}_{11} & -\boldsymbol{K}_{12} & \cdots & 0 \\ -\boldsymbol{K}_{12}^T & \boldsymbol{K}_{22} & \cdots & 0 \\ \vdots & \vdots & \ddots & \vdots \\ 0 & 0 & \ldots & \boldsymbol{K}_{\mathrm{nn}} \end{pmatrix} \tag{12}$$

where $\boldsymbol{K}_{ij}$ includes the effect of the rotational spring at the hinge and root. For an ideal spherical joint, the constraint Jacobian is $\Phi = [\Phi_{ri}, 0, \Phi_{rj}, 0]$, with $\Phi_{ri} = -\mathbf{1}_3$ and $\Phi_{rj} = \mathbf{1}_3$.

Component Model Reduction

In this section, we obtain an expression of the reduced set of multiflexible body dynamics equations. The algorithm makes use of the singular value decomposition (SVD) to project the equations of motion of the constrained system into the tangent subspace of the motion because this method eliminates reaction forces and torques between pairs of interacting bodies in a straightforward manner.[2] The equations of motion with the constraints can be written as

$$\boldsymbol{M}\ddot{\boldsymbol{\eta}} + \boldsymbol{\Phi}_q^T\boldsymbol{\lambda} = \boldsymbol{g} \tag{13}$$

together with $\boldsymbol{\Phi}_q\dot{\boldsymbol{\eta}} = \boldsymbol{\nu}(t)$ and $\boldsymbol{\Phi}_q\ddot{\boldsymbol{\eta}} = \boldsymbol{\gamma}(t)$. By introducing a coordinate transformation $\boldsymbol{P}$ such that

$$\boldsymbol{\eta} = \boldsymbol{P}\boldsymbol{q}_r = (\boldsymbol{P}_1 \quad \boldsymbol{P}_2)(\boldsymbol{q}_{r1} \quad \boldsymbol{q}_{r2})^T \tag{14}$$

one obtains a projection of the dynamics of the constrained system in a direction tangent to the constraint manifold. The matrix $\boldsymbol{P}$ maps the minimal system state $\boldsymbol{q}_r$ into the global system state $\boldsymbol{\eta}$, which means that the projected system moves in the direction of the kinematically admissible displacements, and the effect of the constraints on the balance of forces vanishes. This transformation is equivalent to the one obtained via a SVD of the constraint Jacobian such that $\boldsymbol{\Phi}_q\boldsymbol{P}_1$ is invertible and $\boldsymbol{P}_2^T\boldsymbol{\Phi}_q^T = 0$. Therefore, by premultiplying the equations of motion of each appendage by $\boldsymbol{P}_2$ we have a way to eliminate the reaction forces from the equations of motion. This elimination process is exact; however, it requires some extra computation at each integration time because the algebraic operations required by the SVD can be time consuming. This overhead is a marginal problem because this computation is carried out offline before the dynamic simulation is carried out. Rearranging the equations, we obtain the reduced model of the appendage as

$$\boldsymbol{M}_r\ddot{\boldsymbol{q}}_r + \boldsymbol{K}_r\boldsymbol{q}_r = \boldsymbol{f}_r \tag{15}$$

where the vector $\boldsymbol{q}_r$ (of length n_r) contains the reduced nodal displacements and rotations of each node in global coordinates and $\boldsymbol{f}_r$ represents the vector of generalized external forces on the appendage nodes.

Next, we must couple the base-body equations with the appendage multibody equations. The wheel can be seen as a freely rotating body that is coupled to the base structure via a revolute joint. We assume

that there exists a finite element model of the base structure. The wheel can be modeled with a localized inertia at a particular node, where the degree of freedom corresponding to the wheel rotation is left free. The equations of motion of the rigid spacecraft bus (superscript 1) and of node w (location of reaction wheel) are as follows:

$$\boldsymbol{M}^1\ddot{\boldsymbol{d}} + \boldsymbol{S}^1\dot{\boldsymbol{\omega}} = \boldsymbol{f}_1 \tag{16}$$

$$\boldsymbol{S}^1\ddot{\boldsymbol{d}} + \boldsymbol{J}^1\dot{\boldsymbol{\omega}} + \boldsymbol{J}_w^w\dot{\boldsymbol{\Omega}} + \boldsymbol{G}^i(\boldsymbol{H}^w)\boldsymbol{\omega} + \boldsymbol{\omega}\times(\boldsymbol{J}^1\boldsymbol{\omega}) = \boldsymbol{\tau}_1 \tag{17}$$

$$\boldsymbol{J}_w^w\dot{\boldsymbol{\omega}} + \boldsymbol{J}_w^w\dot{\boldsymbol{\Omega}} = \boldsymbol{\tau}_w^w \tag{18}$$

where the skew-symmetric gyroscopic matrix $\boldsymbol{G}^i(\boldsymbol{H}^w)$ depends on the relative angular momentum $\boldsymbol{H}^w$ present at node w. The equations of motion for the spacecraft in global coordinates can be written as $\boldsymbol{M}_g\ddot{\boldsymbol{q}} + (\boldsymbol{G}_g + \boldsymbol{D}_g)\dot{\boldsymbol{q}} + \boldsymbol{K}_g\boldsymbol{q} = \boldsymbol{u}$, where now the vector $\boldsymbol{q}$ (of length $n_g + 1$) contains the nodal displacements and rotations of each node in global coordinates plus the reaction-wheel rotation angles plus the degrees of freedom of the bus. The global equations need to be reduced from the global set n_g to a set of independent degrees of freedom n_e, and this is done by a transformation $\boldsymbol{q} = \boldsymbol{T}\boldsymbol{q}_e$, where $\boldsymbol{T}$ is of dimension $n_g \times n_e$. Splitting the equations in elastic e and rigid r coordinates, we have

$$\begin{aligned}\boldsymbol{M}_{\mathrm{ee}}\ddot{\boldsymbol{q}}_e + \boldsymbol{M}_{\mathrm{er}}\dot{\boldsymbol{\Omega}} + (\boldsymbol{G}_{\mathrm{ee}} + \boldsymbol{D}_{\mathrm{ee}})\dot{\boldsymbol{q}}_e + \boldsymbol{K}_{\mathrm{ee}}\boldsymbol{q}_e &= \boldsymbol{f}_e \\ \boldsymbol{M}_{\mathrm{re}}\ddot{\boldsymbol{q}}_e + \boldsymbol{M}_{\mathrm{rr}}\dot{\boldsymbol{\Omega}} &= \boldsymbol{f}_r\end{aligned} \tag{19}$$

where now $\boldsymbol{M}_{\mathrm{ee}} = \boldsymbol{T}^T\boldsymbol{M}_g\boldsymbol{T}$ and similarly for the other matrices. Assuming small angular rates (so that the nonlinear terms are negligible, and the modes are still the massnormalized undamped modes) and introducing $\boldsymbol{\Lambda}$ as the diagonal matrix of natural frequencies and ξ as the modal damping coefficient, we can impose the modal transformation $\boldsymbol{q}_e = \boldsymbol{\varphi}\boldsymbol{\eta}$. In Eq. (19), $M_{\mathrm{re}} = (M_{\mathrm{er}})^T$ is the coupling inertia term, and $\boldsymbol{f}_r$ is the vector of the wheel disturbance forces and torques on the bus, plus the reaction wheel actuation torques. Introducing the $(2n, 1)$ state vector as $\boldsymbol{x} = (\boldsymbol{\eta}, \boldsymbol{\beta}, \boldsymbol{\eta}, \boldsymbol{\Omega})^T$, the state-space model can be written as $\dot{\boldsymbol{x}} = \boldsymbol{A}\boldsymbol{x} + \boldsymbol{B}\boldsymbol{u}$ and $\boldsymbol{y} = \boldsymbol{C}\boldsymbol{x} + \boldsymbol{D}\boldsymbol{u}$, where $\boldsymbol{u}$ is the vector of inputs (reaction-wheel torque at location w), and $\boldsymbol{C}$ is the observation matrix. The state matrices are as follows:

$$\boldsymbol{A} = \begin{bmatrix} \boldsymbol{0} & \boldsymbol{1}_{2n} \\ -\boldsymbol{M}^{-1}\boldsymbol{K} & -\boldsymbol{M}^{-1}(\boldsymbol{G}+\boldsymbol{D}) \end{bmatrix} \tag{20}$$

$$\boldsymbol{M} = \begin{bmatrix} \boldsymbol{1}_{n_e} & \boldsymbol{\varphi}^T\boldsymbol{M}_{\mathrm{er}} \\ \boldsymbol{M}_{\mathrm{er}}\boldsymbol{\varphi} & \boldsymbol{M}_{\mathrm{rr}} \end{bmatrix} \tag{21}$$

$$\boldsymbol{K} = \begin{bmatrix} \boldsymbol{K}_{\mathrm{ee}} & \boldsymbol{0} \\ \boldsymbol{0} & \boldsymbol{0} \end{bmatrix} \tag{22}$$

$$\boldsymbol{G}+\boldsymbol{D} = \begin{bmatrix} \boldsymbol{\varphi}^T[\boldsymbol{G}(\boldsymbol{H}^W)]\boldsymbol{\varphi} + 2\boldsymbol{\Lambda}\xi & \boldsymbol{0} \\ \boldsymbol{0} & \boldsymbol{0} \end{bmatrix} \tag{23}$$

$$\boldsymbol{B} = \begin{bmatrix} \boldsymbol{0} \\ -\boldsymbol{\varphi}^T\boldsymbol{T}^T\boldsymbol{b} \\ \boldsymbol{0} \quad \boldsymbol{1}_3 \end{bmatrix} \tag{24}$$

$$\boldsymbol{b} = \begin{bmatrix} \boldsymbol{0} & \boldsymbol{1}_3 & -\boldsymbol{1}_3 \end{bmatrix} \tag{25}$$

$$\boldsymbol{C} = \begin{bmatrix} \boldsymbol{T}\boldsymbol{\varphi} & \boldsymbol{0} & \boldsymbol{0} & \boldsymbol{0} \\ \boldsymbol{0} & \boldsymbol{1}_3 & \boldsymbol{0} & \boldsymbol{0} \\ \boldsymbol{0} & \boldsymbol{0} & \boldsymbol{T}\boldsymbol{\varphi} & \boldsymbol{0} \\ \boldsymbol{0} & \boldsymbol{0} & \boldsymbol{0} & \boldsymbol{1}_3 \end{bmatrix} \tag{26}$$

The eigenspectrum of the whole vehicle, including the rigid rotors, with the eigenspectrum of the dipole and monopole booms, is shown in Table 2.

Table 2 Frequencies of monopole boom, dipole boom, and integrated spacecraft

Mode number	Monopole antenna, Hz	Dipole antenna, Hz	Integrated spacecraft, Hz
1	4.6520 (10^{-1})	7.4665 (10^{-2})	0
2	5.3094 (10^{-1})	8.0674 (10^{-2})	0
3	2.8881 (10^{0})	4.6329 (10^{-1})	0
4	3.2953 (10^{0})	4.9918 (10^{-1})	0
5	7.9910 (10^{0})	1.2808 (10^{0})	0
6	9.1007 (10^{0})	1.3750 (10^{0})	0
7	1.5413 (10^{1})	2.4672 (10^{0})	0
8	1.7492 (10^{1})	2.6361 (10^{0})	0
9	2.4978 (10^{1})	3.9911 (10^{0})	0
10	2.8198 (10^{1})	4.2400 (10^{0})	8.3576 (10^{-2})
11	3.6405 (10^{1})	5.8032 (10^{0})	8.3622 (10^{-2})
12	4.0811 (10^{1})	6.1245 (10^{0})	9.2160 (10^{-2})
13	4.9327 (10^{1})	7.8385 (10^{0})	9.2296 (10^{-2})
14	4.9637 (10^{1})	8.2126 (10^{0})	4.6538 (10^{-1})
15	5.4800 (10^{1})	1.0013 (10^{1})	5.5043 (10^{-1})
16	6.3255 (10^{1})	1.0411 (10^{1})	5.5049 (10^{-1})
17	6.9500 (10^{1})	1.2219 (10^{1})	5.9554 (10^{-1})
18	7.7556 (10^{1})	1.2608 (10^{1})	6.5555 (10^{-1})
19	8.4104 (10^{1})	1.4328 (10^{1})	6.5570 (10^{-1})
20	9.1426 (10^{1})	1.4677 (10^{1})	8.8626 (10^{-1})
21	——	——	8.8745 (10^{-1})
22	——	——	1.6327 (10^{0})
23	——	——	1.6327 (10^{0})
24	——	——	1.8755 (10^{0})
25	——	——	1.8761 (10^{0})
26	——	——	2.6495 (10^{0})
27	——	——	2.6497 (10^{0})
28	——	——	2.8885 (10^{0})
29	——	——	3.4789 (10^{0})

Table 3 Reaction-wheel control gains

Direction	Proportional gain, Nm/rad	Derivative gain, Nms/rad
Roll	1.7028 (10^2)	3.9582 (10^2)
Pitch	1.7028 (10^2)	3.9582 (10^2)
Yaw	4.7300 (10)	1.0995 (10^2)

Control Laws

The control laws used for the spacecraft are of the proportional-plus-derivative-plus-feedforward type. The translation control actually implemented on the spacecraft is of the form

$$\boldsymbol{f}_a = \boldsymbol{K}_p(\boldsymbol{p}_{\mathrm{cmd}} - \boldsymbol{p}_{\mathrm{est}}) + \boldsymbol{K}_v(\boldsymbol{v}_{\mathrm{cmd}} - \boldsymbol{v}_{\mathrm{est}}) + \boldsymbol{M}^i\boldsymbol{a}_{\mathrm{cmd}} \tag{27}$$

The rotational control instead is of the following form:

$$\boldsymbol{\tau}_a = \boldsymbol{\Gamma}_p[\boldsymbol{\lambda}(\boldsymbol{\theta}_{\mathrm{err}})_{\mathrm{cmd}} - \boldsymbol{\lambda}(\boldsymbol{\theta}_{\mathrm{err}})_{\mathrm{est}}] + \boldsymbol{\Gamma}_v(\boldsymbol{\omega}_{\mathrm{cmd}} - \boldsymbol{\omega}_{\mathrm{est}}) + \boldsymbol{J}^1\boldsymbol{\alpha}_{\mathrm{cmd}} \tag{28}$$

The desired control forces and torques are subsequently fed to the reaction-wheel selection logic. The torque command is distributed on the reaction wheels depending on their orientation in the spacecraft body frame. The reaction-wheel control gains are presented in Table 3. On account of the closed reaction-wheel loops, the eigenstructure for a model with four modes becomes as shown in Table 4. The comparison between the open loop vs the experimental frequencies, shown in Table 4, is not excellent but adequate for the purposes of this study.

Numerical Simulations

A numerical simulation has been carried out to show the performance of the model. The spacecraft bus is given an excitation by a reaction-wheel torque pulse of 0.33 Nm for a duration of 6 s about the bus Z axis (pitch). This input represents a command to slew the spacecraft about the pitch axis, which is a typical maneuver frequently done to maintain the antennas pointed to the ground for

Table 4 Comparison of open-loop, closed-loop, and experimental frequencies

Mode number	Open-loop pole, Hz	Closed-loop pole, Hz	Experimental, Hz
7	0	5.9197 (10^{-2})	0
8	0	8.3560 (10^{-2})	0
9	0	8.3605 (10^{-2})	0
10	8.3576 (10^{-2})	9.2141 (10^{-2})	7.80 (10^{-2})
11	8.3622 (10^{-2})	9.2277 (10^{-2})	8.10 (10^{-2})
12	9.2160 (10^{-2})	1.4400	N/A
13	9.2296 (10^{-2})	4.2351	N/A

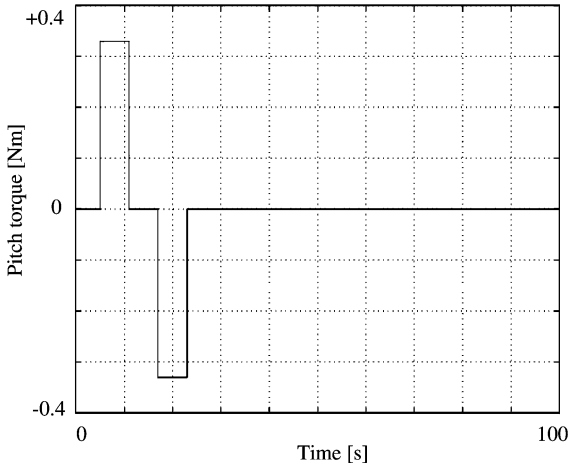

Fig. 2 Applied pitch reaction-wheel torque vs time.

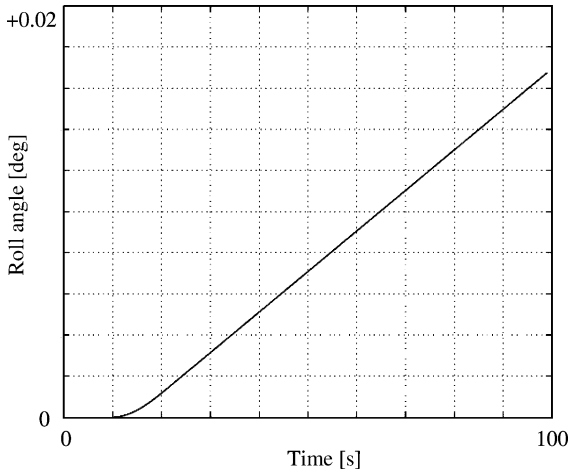

Fig. 3 Roll angle vs time with no feedback (2% damping).

maximum signal reception. Axes X (roll) and Y (yaw) are not actuated. A closed-loop proportional-derivative controller from spacecraft angles and angular rates to spacecraft body torques is applied to maintain the monopole antenna and Y axis always pointed along the nadir direction (local Mars vertical). Ideal (noiseless) sensors are modeled, such as accelerometers and gyros on board the spacecraft bus. Two levels (2 and 5%) of boom structural damping were used in the simulations. Figure 2 depicts the torque profile applied to the pitch axis, designed to excite the 0.083-Hz mode. Figures 3–5 depict the open-loop response of the system (roll, yaw, and pitch angle) to the torque input with 2% damping. One can see that the pitch angle follows a step response, whereas the roll and yaw angles are essentially unaffected. Figure 6–8 show the roll, yaw, and pitch angles of the bus with 2% structural damping applied to the monopole and dipole booms, with the control loops closed. The pitch-axis reaction-wheel speed during the transient maneuver reaches approximately

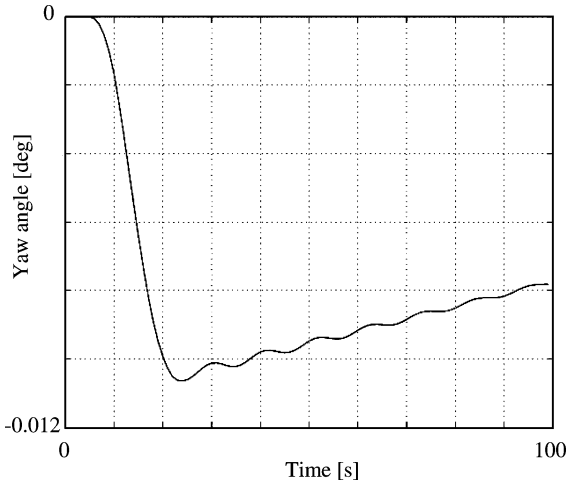

Fig. 4 Yaw angle vs time with no feedback (2% damping).

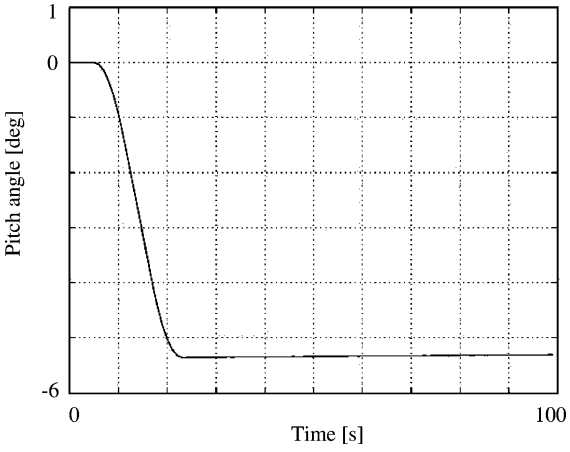

Fig. 5 Pitch angle vs time with no feedback (2% damping).

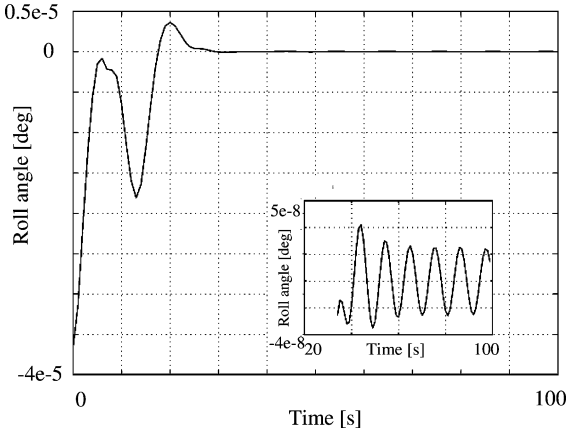

Fig. 6 Roll angle with 2% damping and feedback.

475 rpm (the spin inertia of each wheel is 0.2 kg m^2) for a change in angular momentum of 1.66 Nms. The maximum momentum storage capability of each reaction wheel is 10 Nms. With the reaction-wheel control loops closed, the disturbed response of the spacecraft bus to a pitch-axis symmetric torque pulse waveform of ± 2 Nms (± 0.33 Nm for 6 s) was settled within 10 s following the end of the symmetric input disturbance, as one can appreciate from Fig. 5. This disturbance torque profile was deliberately designed to excite the 20-m boom fundamental mode of 0.0835 Hz (measured with the attitude loops open) and also have a net zero momentum transfer to the bus and zero steady-state rate. The residual settling oscillations after 10 s had amplitudes of sub-arc-seconds with a frequency of

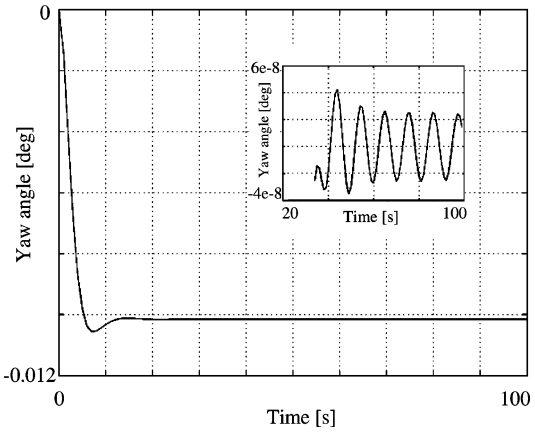

Fig. 7 Yaw angle with 2% damping and feedback.

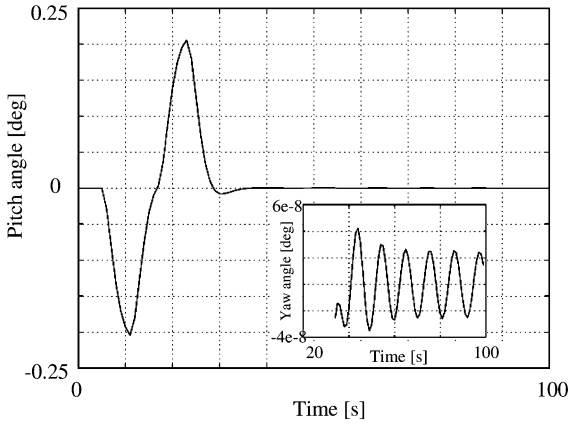

Fig. 8 Pitch angle with 2% damping and feedback.

0.125 Hz, which can be appreciated in the yaw response in Fig. 4. The residual oscillations had damping decrements of 40 s for 50% peak amplitude decay with the 5% structural damping factor, and 55 s with the 2% damping factor. The closed-loop peak bus motion for both damping coefficients was ± 0.2 deg in pitch motion, as shown in Fig. 8. Apparently, the reaction-wheel closed-loop damping of the disturbed bus was far more effective in controlling its settling motion than the structural damping, an expected result for such low-frequency appendage dynamics.

As predicted from boundary condition theory for cantilevered beams, the resulting open-loop oscillatory dynamics of the spacecraft central body are significantly (about 12%) higher in frequency (0.0835 Hz) then the individual 20-m boom modal dynamics of 0.0746 Hz. Following the imposed disturbance, the open-loop settling time with 2% damping to a peak-peak oscillation of about 0.002 deg was about 77 s. With the attitude-control-system reaction wheels in a closed-loop mode, the corresponding settling time to sub-arc-second stability in the *LVLH* Mars centered frame was very short (about 10 s). With the system in a closed-loop mode, the effective inertial stiffness was increased and the bus settling oscillation frequency was about 50% higher at 0.125 Hz compared to the open-loop condition.

Conclusions

The Mars Advanced Radar for Subsurface and Ionospheric Mapping (MARSIS) flexible multibody boom modeling and component model reduction effort was described in this paper. The modeling was necessary to determine the pointing accuracy achievable by the spacecraft during a pitch maneuver at the pericenter of a Martian orbit. From the analysis conducted in this paper, we concluded that the MARSIS booms have open-loop dynamic properties compatible with the Mars Express Spacecraft.

Furthermore, we were able to predict that a realistically sized reaction-wheel controller was able to suppress the antenna residual transient vibration dynamics so that it contributed negligible error to the mission science pointing accuracy and jitter (line-of-sight stability) capabilities.

Acknowledgments

The authors gratefully acknowledge the detailed technical information provided by personnel at TRW Astro Aerospace, Goleta and Carpenteria, California, and with the Mars Express Project at Astrium, Toulouse, France. We also extend our appreciation to the Jet Propulsion Laboratory (JPL) Mars Advanced Radar for Subsurface and Ionospheric Mapping Experiment project managers who encouraged our independent examination of the design, modeling, and testing of the antenna booms to establish the highest confidence in its deployment and in-flight dynamics compatibility with the Mars Express mission. Finally, we wish to acknowledge our JPL colleague, Jeff Umland, for his helpful technical discussions.

References

[1]Woodard, S. E., Lay, R. R., Jarnot, R. F., and Gell, D. A., "Experimental Investigation of Spacecraft In-Flight Disturbances and Dynamic Response," *Journal of Spacecraft and Rockets*, Vol. 34, No. 2, 1997, pp. 199–204.

[2]Grewal, A., and Modi, V. J., "Multibody Dynamics and Robust Control of Flexible Spacecraft," *IEEE Transactions on Aerospace and Electronic Systems*, Vol. 36, No. 2, 2000, pp. 491–500.

[3]Kelkar, A., "Mathematical Modeling of a Class of Multibody Flexible Space Structures," NASA TM 109166, Dec. 1994.

[4]Mosier, G., Parrish, K., Fermiano, M., Redding, D., Kissil, A., Papalexandris, M., Craig, L., Page, T., and Shunk, R., "NGST Performance Analysis Using Integrated Modeling," Next Generation Space Telescope Monograph, No. 6, Aug. 2000, URL: http://www.jwst.nasa.gov/doclist/bytitle.html.

[5]Quadrelli, M., and Sirlin, S., "Modeling and Control of Membranes for Gossamer Spacecraft," AIAA Paper 2001-1201, April 2001.

[6]Harris, C. M. (ed.), *Shock and Vibration Handbook*, 4th ed., McGraw–Hill, New York, 1996, Chap. 7.

C. Kluever
Associate Editor